catalysts

MDPI

Article

Constructing Z-Scheme 0D/2D TiO_2 Nanoparticles/Bi_2O_3 Nanosheet Heterojunctions with Enhanced Visible Light Induced Photocatalytic Antibiotics Degradation and Hydrogen Evolution

Lijia Xie [1], Piaopiao Wu [1], Qiong Lei [2], Chong Xu [1], Weiya Huang [1,*], Xunjun Chen [1], Kai Yang [1] and Hua He [3]

[1] Faculty of Materials, Metallurgical and Chemistry, Jiangxi University of Science and Technology, Ganzhou 341000, China
[2] Ganzhou Center for Disease Control and Prevention, Ganzhou 341000, China
[3] Department of Laboratory Medicine, First Affiliated Hospital of Gannan Medical University, Ganzhou 341000, China
* Correspondence: hweiya@126.com

Abstract: Photocatalysis has been regarded as a promising technology for degrading organic pollutants in wastewater and producing hydrogen. In this paper, TiO_2 nanoparticles (NPs) were synthesized to improve the visible light absorption of TiO_2, which were further combined with Bi_2O_3 nanosheets to synthesize a series of 0D/2D TiO_2 NPs/Bi_2O_3 nanosheet heterojunctions. The visible light induced photocatalytic activities of the as-synthesized TiO_2/Bi_2O_3 heterojunctions were studied. The optimized catalyst TB-3 with 15 wt% of Bi_2O_3/TiO_2 exhibited the best photocatalytic degradation of tetracycline hydrochloride (TC). The degradation rate constant k of TC over TB-3 was approximately eight times and 39 times greater than that of P25 and Bi_2O_3, respectively. Additionally, TB-3 showed the highest amount of hydrogen evolution, while that of Bi_2O_3 was almost zero. The enhancement of photocatalytic performances was ascribed to the improved visible light absorption and the Z-scheme charge transfer path of the TiO_2/Bi_2O_3 heterojunctions, which enhanced the separation efficiency and reduced recombination of photogenerated charge carries, as evidenced by UV–Visible diffuse reflectance spectroscopy (DRS), photoluminescence spectroscopy (PL), and electrochemistry measurements. The active species trapping experiments and the electron spin resonance (ESR) results revealed that $\cdot O_2^-$ was the main active substance in the photocatalytic degradation. The possible degradation pathway and intermediate products of TC have been proposed. This work provides experimental evidence supporting the construction of Z-scheme heterojunctions to achieve excellent visible light induced photocatalytic activity.

Keywords: photocatalysis; 0D/2D heterojunctions; antibiotics degradation; hydrogen evolution; wastewater treatment

check for updates

Citation: Xie, L.; Wu, P.; Lei, Q.; Xu, C.; Huang, W.; Chen, X.; Yang, K.; He, H. Constructing Z-Scheme 0D/2D TiO_2 Nanoparticles/Bi_2O_3 Nanosheet Heterojunctions with Enhanced Visible Light Induced Photocatalytic Antibiotics Degradation and Hydrogen Evolution. *Catalysts* **2023**, *13*, 583. https://doi.org/10.3390/catal13030583

Academic Editors: Roberto Fiorenza and Detlef W. Bahnemann

Received: 6 January 2023
Revised: 8 March 2023
Accepted: 9 March 2023
Published: 14 March 2023

1. Introduction

Recently, increasing energy shortage and environmental pollution are two serious problems confronting the sustainable development of human society [1]. To alleviate both environmental pollution and energy crisis, semiconductor photocatalysis, which is capable of using renewable solar energy to remove pollutants in wastewater and produce hydrogen, is considered as an ideal way among various technologies in environmental and energy fields [1,2]. Antibiotics, as a kind of emerging pollutant, have attracted extensive attention due to their increasing production and consumption [3]. The presence of antibiotics and their metabolites in natural water contributes to the development of antibiotic resistant genes and bacteria, which poses a serious threat to the ecological environment, and even human health [4]. Thus, it is of great significance to efficiently remove antibiotics from wastewater by using photocatalysis.

However, the extensive application of photocatalysis is greatly limited by the high recombination rate of photogenerated charge carriers and low solar energy utilization efficiency. To achieve an efficient photocatalytic reaction of pollutant degradation and hydrogen evolution, photocatalysts with excellent visible light absorption and superior efficiencies of charge transfer and separation are highly required. Constructing Z-scheme heterojunctions between semiconductors is believed to be an effective way to fabricate novel photocatalysts with efficient photocatalytic activities [5–8]. In a Z-scheme photocatalytic system, the recombination of charge carriers can be efficiently suppressed by combining photogenerated electrons on the conduction band (CB) of one semiconductor and holes on the valence band (VB) of another semiconductor. The remaining electrons on CB and the holes on VB have a relatively stronger redox ability, and their participation in photocatalytic reactions results in a higher photocatalytic activity than that of a single semiconductor. Thus, several Z-scheme heterojunctions including ZnS/SnS_2 [9], $CeO_2/BiOBr$ [10], and MoO_3/Bi_2O_4 [11] have shown efficient photocatalytic performance for antibiotic removal from wastewater.

Titanium dioxide (TiO_2) is a typical semiconductor that has been widely applied as one of the candidates to fabricate heterojunctions with other semiconductors due to its low cost, non-toxicity, chemical stability, and commercial availability [12]. However, the broad energy band gap of TiO_2 (~3.2 eV) results in the low utilization of solar energy and unsatisfied photocatalytic activity under visible light, which inhibits its practical application in photocatalysis. The preparation of TiO_2 nanoparticles (NPs) by morphology control is an effective method to improve the photocatalytic activity of TiO_2. Compared with large-particle TiO_2, TiO_2 NPs have higher photocatalytic activities due to their larger specific surface area, smaller size, and narrower band gap [13]. On the other hand, Bi_2O_3 is an important N-type metal oxide semiconductor with a relatively lower band gap of ~2.8 eV, which can be excited by visible light [14,15]. Various heterojunctions based on Bi_2O_3 have been used as visible light induced photocatalysts with greatly enhanced photocatalytic activities [16–18]. For example, Liu deposited Bi/Bi_2O_3 nanoparticles on the surface of TiO_2 nanotube arrays, and the resulting Z-scheme $Bi/Bi_2O_3/TiO_2$ showed increased light absorption capacity and boosted photocatalytic activity [17]. Zhou et al. fabricated a series of $Bi_2O_3/C_3N_4/TiO_2$@C heterojunctions with enhanced antibiotic removal efficiency, which was a result of the unique double Z-scheme pathway of the photogenerated charge carriers [18]. Thus, the development of Z-scheme Bi_2O_3/TiO_2 heterojunctions is expected to obtain catalysts with enhanced photocatalytic activities.

Based on the above consideration, TiO_2 NPs were successfully synthesized by a facile sol–gel method to improve the visible light absorption of TiO_2. The obtained TiO_2 NPs were further combined with Bi_2O_3 nanosheets to fabricate a series of 0D/2D TiO_2 NPs/Bi_2O_3 heterojunctions (TB-x, x = 1–4) as efficient catalysts for tetracycline hydrochloride (TC) degradation and hydrogen evolution. The optimized sample TB-3 exhibited the best performances of TC degradation and hydrogen evolution, and such an enhancement of the photocatalytic activity was studied by various characteristics and trapping experiments. A possible Z-scheme heterojunction charge transfer mechanism was proposed.

2. Results and Discussion

2.1. Morphology and Structure

The X-ray diffraction (XRD) spectra of the catalysts are shown in Figure 1. As can be seen, the sample of TiO_2 NPs showed diffraction peaks at 25.5°, 38.0°, 48.2°, 54.0°, 55.2° and 62.9°, which were attributed to the (101), (004), (200), (105), (211), and (204) crystal planes of the anatase-type TiO_2 (JCPDS #99-0008) [19]. The above peaks were also found in the XRD spectra of the TiO_2 NPs/Bi_2O_3 composites TB-x (x = 1–4), indicating the presence of TiO_2 NPs. The intensity of the characteristic diffraction peak corresponding to the (101) crystal plane of TiO_2 decreased gradually from TB-1 to TB-4 due to the decreasing content of TiO_2 NPs in the composites. For pure Bi_2O_3, two peaks located at 27.95° and 32.39° were ascribed to the (201) and (220) crystal planes of β-Bi_2O_3 (JCPDS #27-0050) [20], whilst the diffraction

peaks were weak and broad, indicating the formation of Bi_2O_3 with low crystallinity and small crystallite size [21,22]. These two peaks can also be observed in TB-x (x = 1–4) samples, meaning that the TiO_2 NPs/Bi_2O_3 composites were successfully prepared.

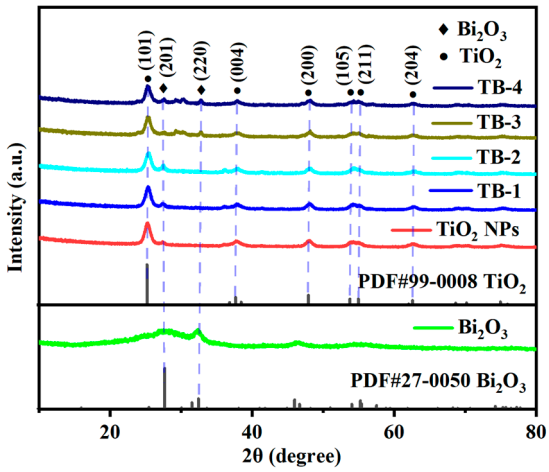

Figure 1. XRD spectra of TiO_2 NPs, Bi_2O_3, and TB-x (x = 1–4).

Figure S1 shows the FTIR spectra of the as-prepared samples. As can be seen for TiO_2 NPs, the broad peak from 3250 cm^{-1} to 3500 cm^{-1} corresponded to the Ti–O–H vibration [23], while the peak in the range of 400 cm^{-1}–600 cm^{-1} belonged to the stretching vibration of Ti–O–Ti [24]. The absorption peak located at 1632 cm^{-1} corresponded to the –OH of adsorbed water [25]. In the FTIR spectrum of pure Bi_2O_3, the absorption peaks at 530 cm^{-1} and 1380 cm^{-1} were the vibrational mode of Bi–O bonds in Bi_2O_3 [20,25]. The main characteristic peaks of TiO_2 NPs and Bi_2O_3 can be observed in TB-x (x = 1–4), which indicates the presence of both Bi_2O_3 and TiO_2 NPs. This further confirms the successful synthesis of the TiO_2 NPs/Bi_2O_3 composites.

The chemical composition and chemical states of elements in TB-3 were further analyzed by X-ray photoelectron spectroscopy (XPS). Figure 2a shows the XPS survey spectrum of TB-3, in which the Bi, Ti, and O elements were detected. In the Ti 2p high-resolution XPS spectrum of TB-3 (Figure 2b), two fitted peaks centered at 458.83 eV and 464.43 eV were attributed to Ti $2p_{3/2}$ and Ti $2p_{1/2}$, respectively. The binding energy difference between the two peaks was around 5.7 eV, indicating the presence of Ti in the form of Ti^{4+} [26]. In Figure 2c, the high-resolution XPS spectrum of Bi 4f showed two strong peaks at 159.23 eV and 164.58 eV, corresponding to the Bi $4f_{7/2}$ and Bi $4f_{5/2}$ electron levels of Bi^{3+} ions in Bi_2O_3 [26]. In Figure 2d, the O 1s peak can be deconvoluted into two different peaks at 529.63 eV and 531.17 eV, which were attributed to the lattice oxygen and surface hydroxyl groups, respectively [27]. Therefore, the above results further confirm the successful formation of Bi_2O_3/TiO_2 heterojunctions in TB-3.

Figure 3a–c shows the SEM images of TiO_2 NPs, Bi_2O_3, and TB-3. The sample of TiO_2 NPs exhibited uniform nanoparticles, while pure Bi_2O_3 was composed of aggregated nanosheets. TB-3 contained both 2D nanosheets and 0D nanoparticles, in which a large number of 0D nanoparticles were deposited on 2D nanosheets to form 0D/2D heterojunctions (Figure 3c). In addition, Figure S2 shows the presence of O (77.98%), Ti (20.2%), and Bi (1.82%) in TB-3, which is further evidenced by elemental mapping images in Figure 3d–g, proving the coexistence of Bi_2O_3 and TiO_2 NPs in TB-3.

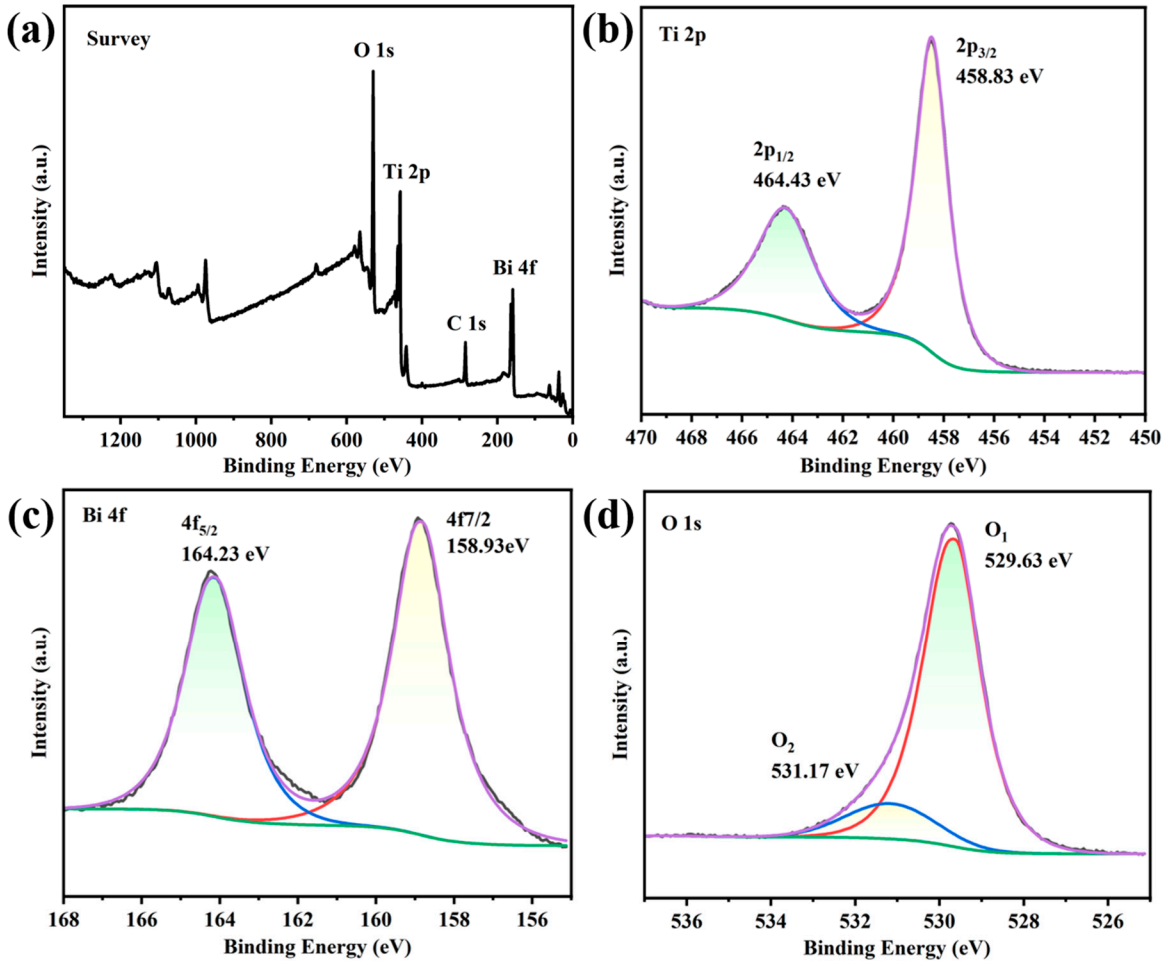

Figure 2. XPS spectra of TB-3: (**a**) survey, (**b**) Ti 2p, (**c**) Bi 4f, and (**d**) O 1s.

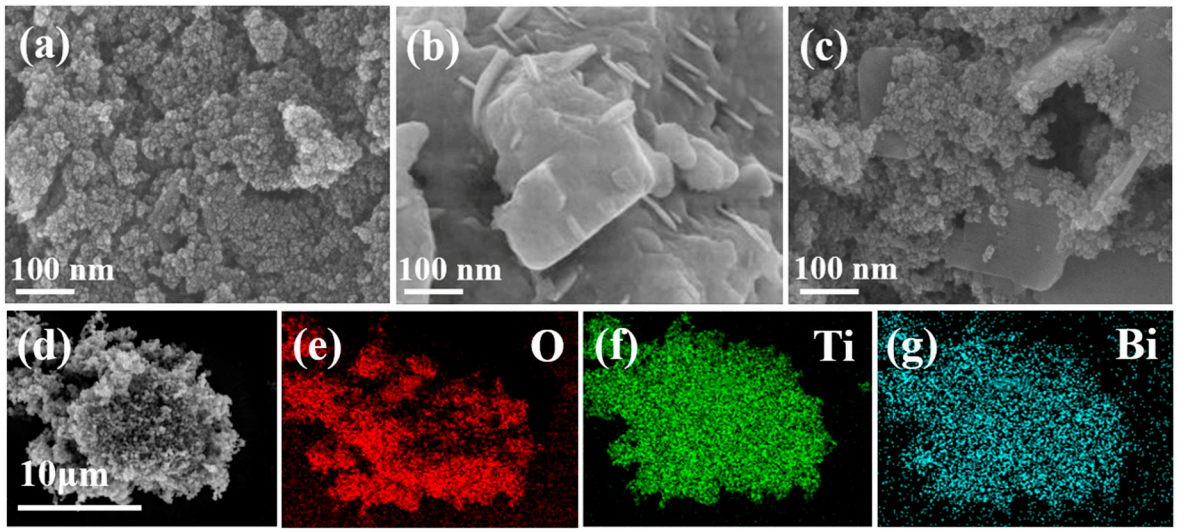

Figure 3. SEM images of (**a**) TiO_2 NPs, (**b**) Bi_2O_3, and (**c**) TB-3; (**d**–**g**) EDS elemental mapping images of TB-3.

Figure 4a,d shows the TEM images of TiO_2 NPs, which displayed nanoparticles with the particle size concentrated at 7.5 nm. The TiO_2 NPs exhibited a lattice fringe with crystal spacing of 0.352 nm, which belonged to the (101) crystal plane of anatase TiO_2. The sample of Bi_2O_3 demonstrated a nanosheet morphology and the lattice spacing 0.295 nm

was ascribed to the (211) crystal plane of Bi_2O_3 (Figure 4b,e). The TEM images of TB-3 (Figure 4c,f) showed nanosheets with nanoparticles deposited. Two different lattice fringes with a crystal spacing of 0.346 nm and 0.352 nm can be found in Figure 4f, which were ascribed to the (210) crystal plane of Bi_2O_3 and the (101) crystal plane of TiO_2, respectively. This revealed the formation of heterojunctions between the Bi_2O_3 and TiO_2 NPs.

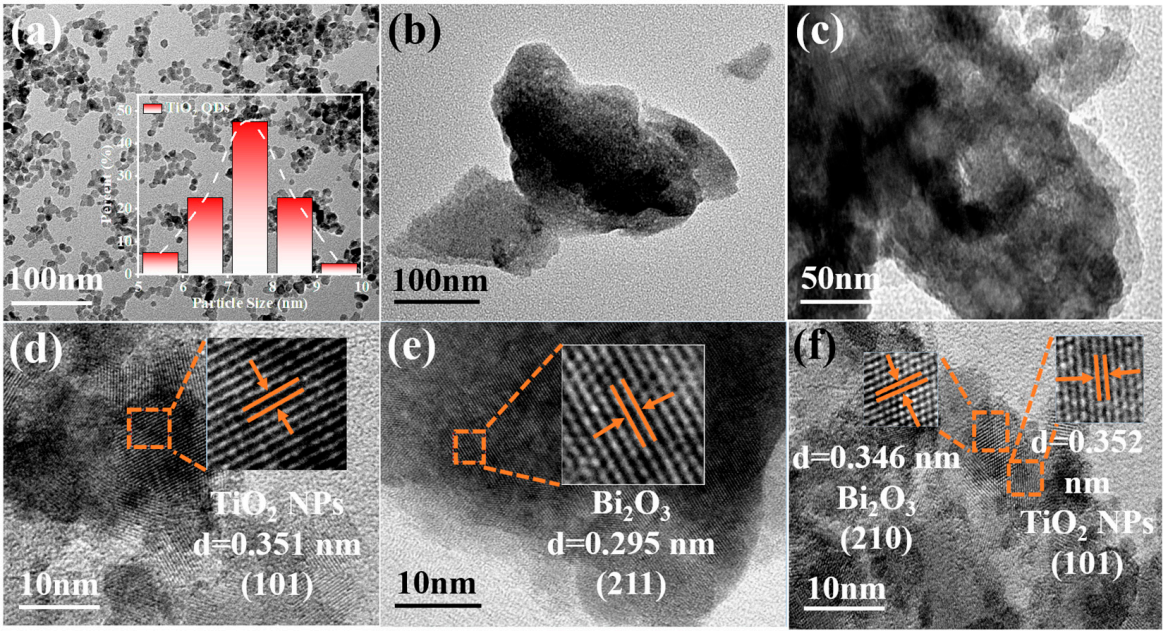

Figure 4. TEM and HR-TEM images of (**a**,**d**) TiO_2 NPs, (**b**,**e**) Bi_2O_3, (**c**,**f**) TB-3.

Figure 5 shows the N_2 adsorption–desorption isotherms and the pore size distribution plots of the as-prepared catalysts. The BET specific surface areas (S_{BET}), average pore sizes, and pore volumes of the samples are shown in Table S1. As can be seen from Figure 5a, the TiO_2 NP and TB-x (x = 1, 2, 3, and 4) composites exhibited typical type IV isotherms and H3 type hysteresis rings, indicating the presence of slit-shaped mesopores [28]. Among them, the sample of TiO_2 NPs exhibited the highest SBET and pore volume, which were 119.87 m^2/g and 0.35 cm^3/g, respectively. The S_{BET} and pore volumes of TB-x (x = 1, 2, 3, 4) were slightly lower than those of the TiO_2 NPs due to the presence of Bi_2O_3, which showed the smallest S_{BET} (5.14 m^2/g) and pore volume (0.036 cm^3/g). It is worth mentioning that TB-3 had a greater S_{BET} and pore volume than those of TB-2 or TB-4, which may provide more exposed active sites to promote the photocatalytic performance.

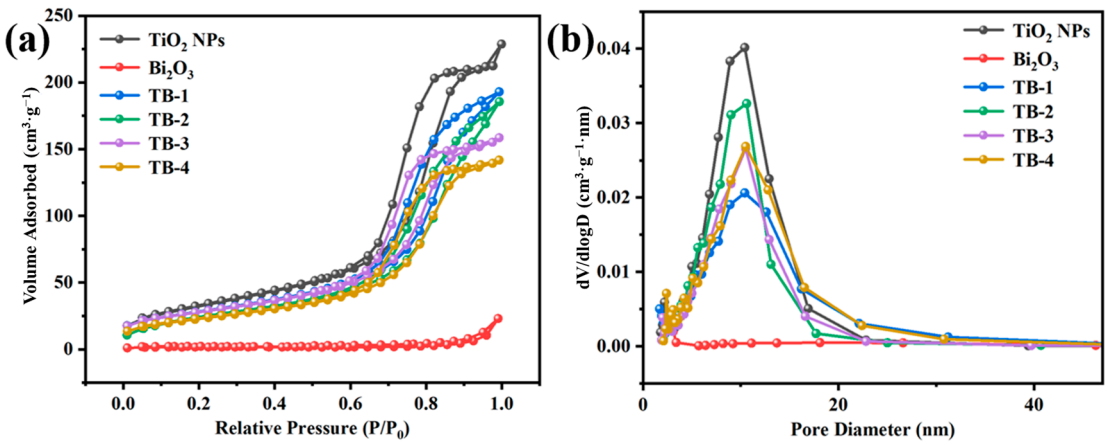

Figure 5. (**a**) N_2 absorption–desorption isotherms, (**b**) corresponding pore size distributions of the TiO_2 NPs, Bi_2O_3, and TB-x (x = 1–4).

2.2. Optical Properties

The UV–vis diffuse reflection spectra (DRS) of TiO_2 NPs, Bi_2O_3, and TB-x (x = 1−4) composites are shown in Figure 6a. Their band gap (E_g) values were determined, as shown in Figure 6b, according to the Tauc equation [29]: $Ah\nu = B(h\nu - E_g)^{n/2}$, where A, hν, and B are the absorption coefficient, incident photon energy, and a constant, respectively. The value of n depends on the type of semiconductor, which is 1 for direct semiconductors and 4 for indirect semiconductors. For all TB-x (x = 1–4) samples, $n = 4$ was applied [30]. The absorption edge of Bi_2O_3 was around 412 nm and its E_g was estimated at 3.03 eV; while the TiO_2 NPs showed an absorption edge at 420 nm with E_g = 2.99 eV. It is obvious that the light absorption range of TiO_2 NPs was significantly enlarged to the visible light region, which is believed to be due to the size effect of the nanoparticles [31,32]. Compared with Bi_2O_3, the adsorption edges of TB-x (x = 1, 2, 3, and 4) displayed a slight red-shift. Importantly, TB-3 showed enhanced absorption in the visible region of 400–500 nm. The E_g values of TB-x (x = 1, 2, 3, and 4) were estimated as 2.96 eV, 2.79 eV, 2.75 eV, and 2.96 eV, respectively. It is obvious that TB-3 possessed the narrowest E_g (2.75 eV) among the four TB-x samples, which is beneficial to improving its visible light absorption property. This result indicates that the band gap of 0D/2D TiO_2 NPs/Bi_2O_3 nanosheet heterojunctions depends on the amount of Bi_2O_3 and TiO_2 in the TB-x composites.

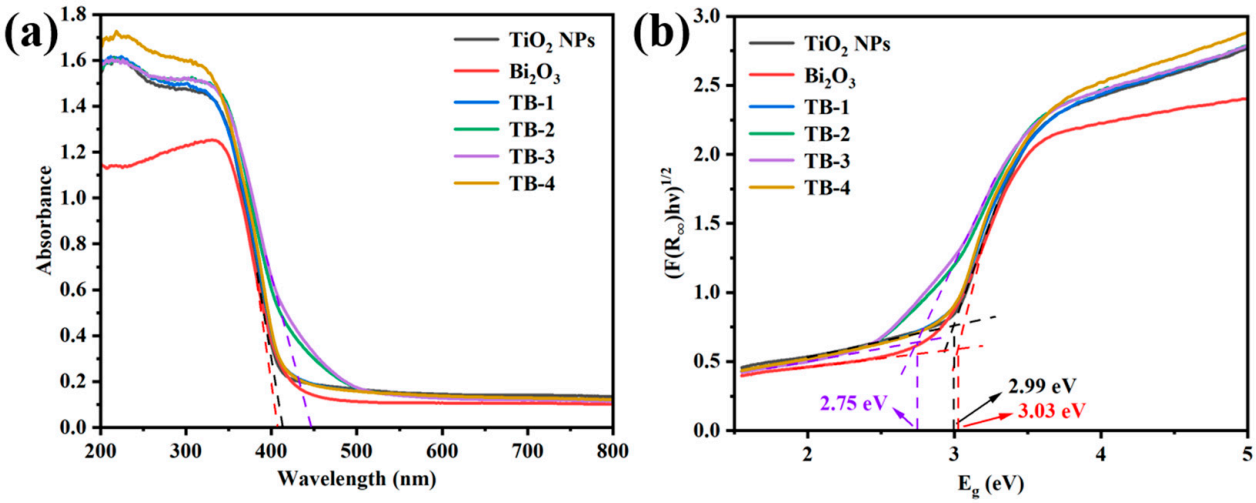

Figure 6. (**a**) UV–Vis DRS and (**b**) Tauc plots of TiO_2 NPs, Bi_2O_3, and TB-x (x = 1–4).

2.3. Photoluminescence and Photoelectrochemical Analysis

Figure 7a shows the photoluminescence (PL) spectra of the TiO_2 NPs, Bi_2O_3, and TB-x (x = 1–4). As fluorescence can be produced by combining photogenerated electrons with holes, the lower intensity of PL means a lower recombination rate of the photogenerated electron-hole pair in the catalysts [33]. As can be seen, Bi_2O_3 exhibited the strongest emission peak concentrated at around 470 nm, indicating the highest combination rate of photogenerated electron-hole pairs in single Bi_2O_3. Compared with Bi_2O_3, the PL intensity of TB-x (x = 1–4) decreased significantly, indicating that the recombination of electron-hole pairs can be reduced due to the formation of Bi_2O_3/TiO_2 NP heterojunctions. It was noted that the PL intensity of TB-3 was much lower than those of the other TB-x (x = 1, 2 and 4) composites, which is beneficial to improving the photocatalytic activity. On the other hand, the intensity of the TiO_2 NPs was the lowest among all of the samples. This may be due to the fact that the size of the TiO_2 NPs was smaller than the mean free path of electrons in TiO_2, which is about 100 nm, resulting in the extremely low recombination rate of photogenerated electron-holes in the TiO_2 NPs [34]. A similar phenomenon has been reported by other research [35].

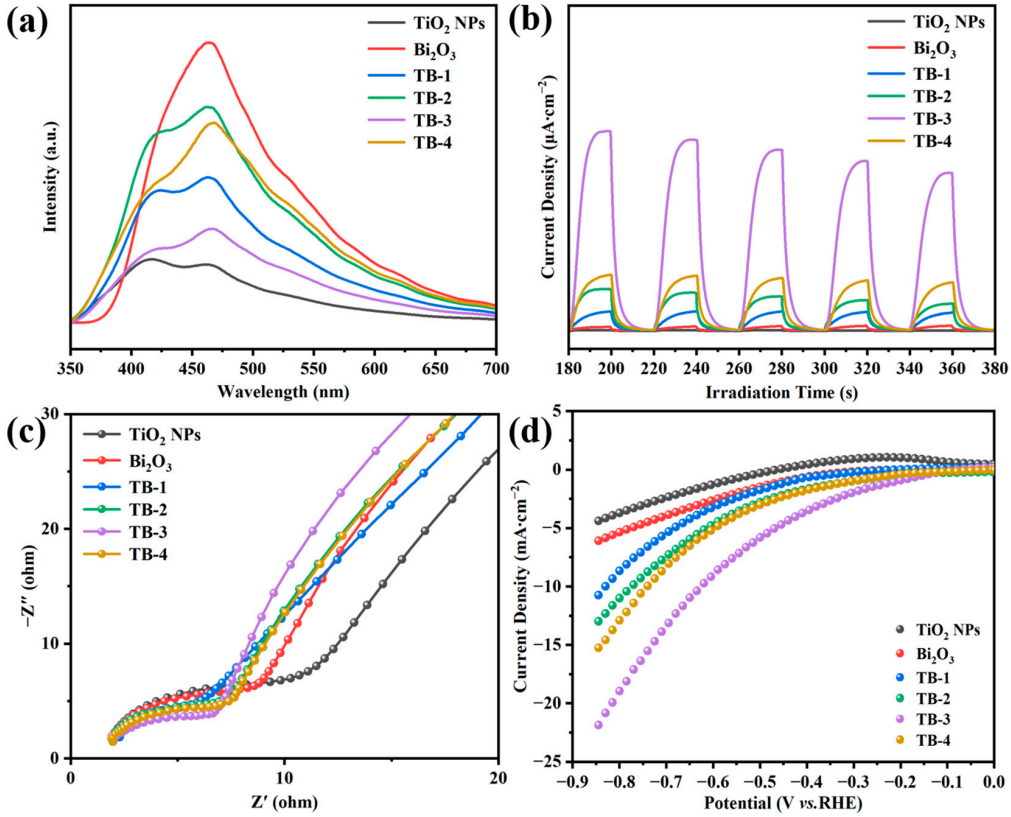

Figure 7. (**a**) Photoluminescence (PL) emission spectra. (**b**) Photocurrent response. (**c**) EIS Nyquist plots, (**d**) LSV curves of TiO_2 NPs, Bi_2O_3, and TB-x (x = 1–4).

In order to further study the migration, transfer, and separation of photogenerated charge carriers, the photoelectrochemical properties of all the as-prepared catalysts were characterized. Figure 7b demonstrates the transient photocurrent responses of the catalysts. Generally speaking, the stronger transient photocurrent response suggests the higher separation and migration efficiency of photo-excited electron-hole pairs [36]. For pure Bi_2O_3 or TiO_2 NPs, the intensity of photocurrent was very low. In contrast, the photocurrent intensity of TB-x (x = 1–4) was significantly enhanced, indicating that the transfer and separation ability of the photogenerated charge carriers could be significantly improved after the formation of heterojunctions between Bi_2O_3 and TiO_2 NPs. In particular, TB-3 had the highest photocurrent intensity among the four TB-x composites, which was expected to have the best photocatalytic performance.

Figure 7c shows the electrochemical impedance spectroscopy (EIS) of the catalysts. The smaller semicircle radius in the Nyquist plots reflects the lower charge transfer resistance [37]. As can be seen, the arc radius of TB-x was in the order of TB-3 < TB-4 < TB-2 < TB-1, which is consistent with the results of the photocurrent responses. Similarly, sample TB-3 had the smallest resistance arc radius, suggesting the lowest charge transfer resistance. Figure 7d shows the linear sweep voltammetry (LSV) curves of the catalysts. At the same current density and scanning rate, a lower overpotential indicates a lower energy dissipation and consequently better electrocatalytic hydrogen production (HER) [38]. Obviously, among all of the catalysts, TB-3 needed the lowest overpotential to drive the same current density, indicating that TB-3 had the best HER performance.

2.4. Photocatalytic Activities

Tetracycline hydrochloride (TC) was selected as a model contaminant, and TC solution with an initial concentration of 50 mg/L was used to investigate the photocatalytic behaviors of the as-prepared catalysts. Prior to visible light irradiation, all of the catalysts were stirred in the dark for 60 min to fully achieve the adsorption–desorption equilibrium.

The removal of TC in the dark was almost unchanged after 50 min (Figure S3a), indicating that the adsorption–desorption equilibrium was reached. The pseudo-first-order and pseudo-second-order kinetic models were used to fit the adsorption data (Figure S3b), and the fitted parameters are shown in Table S2. It was found that the pseudo-second-order kinetic model with the correlation coefficient R^2 = 0.999 described the adsorption process better than that of the pseudo-first-order kinetic model (R^2 = 0.917). This indicates that the adsorption of TC over catalysts is governed by chemisorption [39].

Figure 8a and Figure S4 compare the adsorption and photocatalytic degradation removal of TC over the as-fabricated catalysts; meanwhile, P25 was also studied for comparison. Almost no TC was removed in the dark and under visible light irradiation without the presence of the catalyst, whilst only 5% or 10% TC removal was observed over P25 or Bi_2O_3. In contrast, the total removal of TC was greatly improved to 50% over TiO_2 NPs, which was 10-fold that of P25. When the TiO_2 NPs were combined with Bi_2O_3 to form 0D/2D heterojunctions, the total removal rate of TC over the resulting composite TB-x (x = 1, 2, 3, or 4) was further increased to 65–80%. Among them, TB-3 showed the highest adsorptive and photocatalytic removal rate of TC, indicating the highly efficient TC removal by rationally constructing heterojunctions between TiO_2 NPs and Bi_2O_3. The photocatalytic degradation of TC was fitted into the pseudo-first-order kinetic model, according to the formula $\ln(C/C_0) = -kt$, as shown in Figure 8b. The apparent kinetic rate constant (k) of TB-3 was the highest among all the samples (0.1443), which was 1.86, 8.15, and 39 times greater than that of the TiO_2 NPs, P25, and Bi_2O_3, respectively. Table S3 compares the TC removal efficiency with other TiO_2/Bi_2O_3-based heterojunctions [40–44]. Although the experimental conditions were different, the TB-3 prepared in this work showed a much faster TC removal with comparable removal efficiency, even at a higher initial TC concentration.

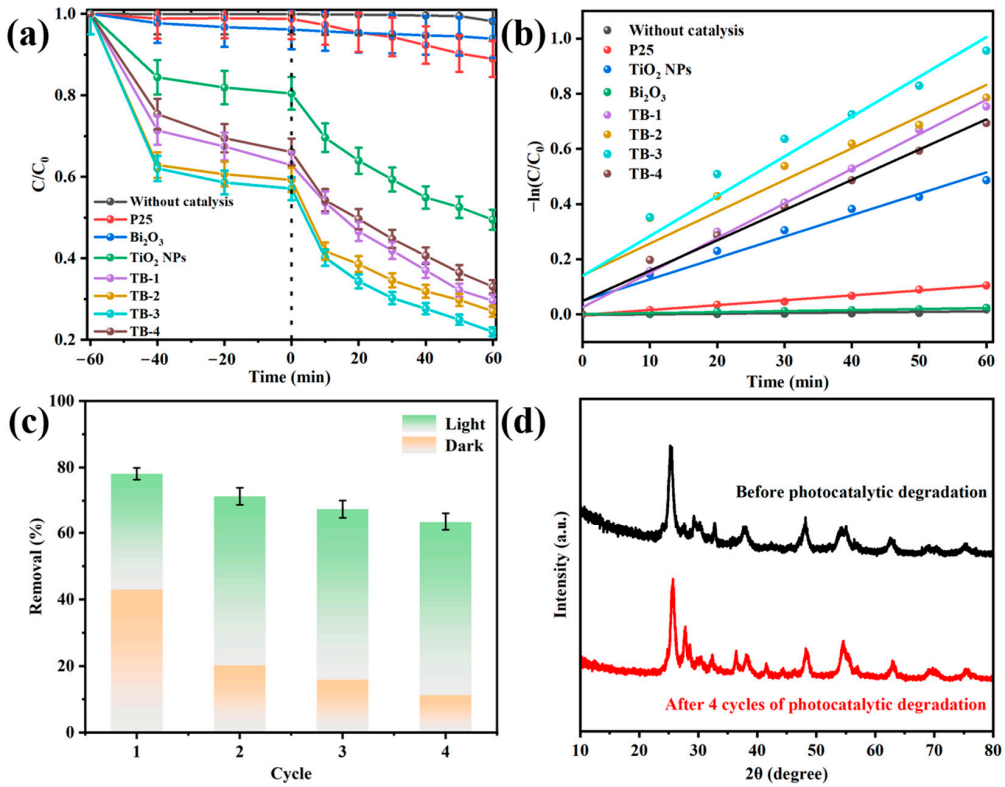

Figure 8. (**a**) Adsorption in the dark and photocatalytic degradation of TC under visible light irradiation by using the as-prepared samples and P25. (**b**) The fitting of the pseudo-first-order kinetic model. (**c**) Cyclic adsorption–photocatalytic degradation of TC over TB-3. (**d**) XRD patterns of TB-3 before and after four cycles.

The cyclic adsorption–photocatalytic degradation of TC was conducted to evaluate the stability of TB-3, as shown in Figure 8c. The synergistic adsorption–photocatalytic TC removal was approximately 80% in the first cycle, while 65% total removal was still achieved in the fourth cycle. The decrease in the total removal of TC mainly resulted from the decline in adsorptive removal, from 50% in the first cycle to 16.4% in the fourth cycles. This is probably because some of the adsorption sites are occupied by TC and its degradation intermediates. However, the TC removal by visible light-induced photocatalytic degradation was almost unchanged, indicating the good stability of TB-3 during the photocatalytic reaction. In addition, the XRD spectra of TB-3 before and after four cycles are compared in Figure 8d. It is clear that no obvious change could be observed in the XRD patterns, which further implies that TB-3 possesses good stability.

The possible intermediate products during the photocatalytic degradation of TC by using TB-3 were studied by HPLC-MS analysis, as shown in Figure 9. The corresponding mass spectra of the intermediate products are highlighted in Figure S5. It can be seen that there were three possible degradation pathways during the TC degradation process involving 12 intermediates with the main mass peaks in the range of *m/z* = 461~246. In pathway I, TC1 (*m/z* = 396) was produced after the dehydration process, loss of amino group, and demethylation at the $–N(CH_3)_2$ bond of the TC molecule, and then underwent further loss of the amino group and dehydroxylation to generate TC2 (*m/z* = 340), which was transformed into TC3 (*m/z* = 279) by a ring opening reaction [45]. Next, TC4 (*m/z* = 246) was produced by the demethylation process [45]. In pathway II, the first intermediate TC5 (*m/z* = 417) was produced by the oxidation of $–CH_3$ to –CHO and deamidation of $–C{=}ONH_2$, while further demethylation and loss of the formyl group led to the formation of TC6 (*m/z* = 374) [46]. Next, the dehydroxylation and ring opening reaction yielded TC7 (*m/z* = 362) and then TC8 (*m/z* = 279) [46]. In pathway III, TC9 (*m/z* = 461) was first generated through dipolar cycloaddition and the rearrangement of the hydroxyl group [47]. Next, TC10 (*m/z* = 453) was formed by demethylation and hydroxylation, and then TC11 (*m/z* = 306) was yielded by dihydroxylation, along with the ring opening reactions [47]. Furthermore, TC12 (*m/z* = 246) was formed by demethylation and the loss of the formyl group [45]. With the extension in the reaction time, the intermediates of TC4, TC8, TC12, and some other intermediate products were finally mineralized into CO_2, H_2O, NH_4^+, and NO_3^-.

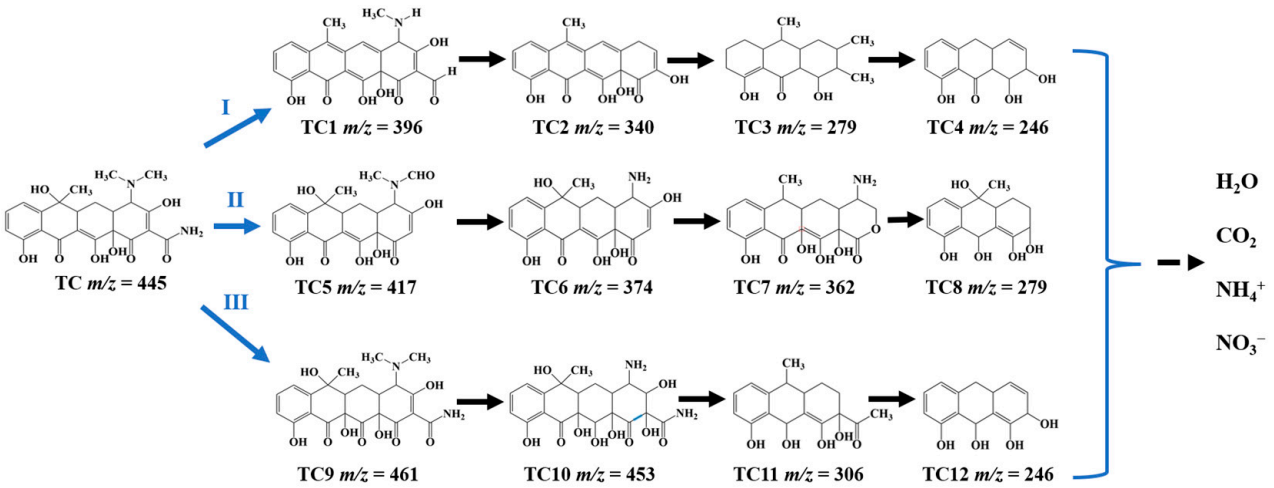

Figure 9. Intermediates and the possible photocatalytic degradation pathways for TC removal using TB-3.

Figure 10 shows the amount of hydrogen produced via the hydrogen evolution reaction (HER) using TiO_2 NPs, Bi_2O_3, and TB-x (x = 1–4) under visible light irradiation. Similarly, the hydrogen produced by TB-3 (99.39 $\mu mol \cdot g^{-1}$) was the highest among all the samples including TiO_2 NPs (76.15 $\mu mol \cdot g^{-1}$). However, nearly no hydrogen was produced

by pure Bi_2O_3, probably due to the insufficient reduction ability of photogenerated electrons on the conductive band of Bi_2O_3. This further confirms the enhanced photocatalytic reduction activity of TB-3 due to the construction of the 0D/2D TiO_2 NPs/Bi_2O_3 nanosheet heterojunctions.

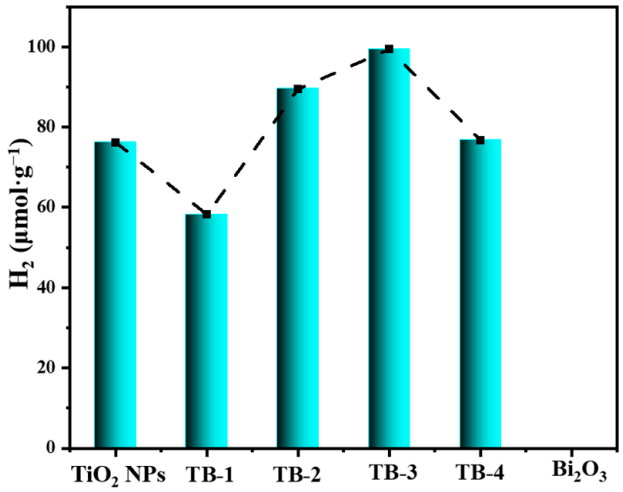

Figure 10. Photocatalytic hydrogen production of TiO_2 NPs, Bi_2O_3, and TB-x (x = 1–4).

2.5. Discussion on Photocatalytic Mechanisms

Figure 11 shows the Mott–Schottky curves of the TiO_2 NPs and Bi_2O_3. The positive slope of the curves indicates that both the TiO_2 NPs and Bi_2O_3 were n-type semiconductors [48]. For the n-type semiconductors, the values of the conduction band (CB) were close to their flat band potential, which could be obtained by extrapolating the linear part of the curves to intersect the *X*-axis [48]. Obviously, the CB values of the TiO_2 NPs and Bi_2O_3 were found at −0.5 V (vs. NHE) and 0.33 V (vs. NHE), respectively. The valence bands (VB) of semiconductors were calculated according to the formula $E_{VB} = E_{CB} + E_g$ [36]. The values of E_g were obtained by the DRS results (Figure 5), which were 2.99 V for the TiO_2 NPs and 3.03 V for Bi_2O_3, respectively. Therefore, the VB values of the TiO_2 NPs and Bi_2O_3 were calculated as 2.49 V (vs. NHE) and 3.36 V (vs. NHE), respectively. The values of E_g were obtained by the DRS results (Figure 5), which were 2.99 V for the TiO_2 NPs and 3.03 V for Bi_2O_3, respectively. Therefore, the VB values of TiO_2 and Bi_2O_3 were calculated as 2.49 V (vs. NHE) and 3.36 V (vs. NHE), respectively.

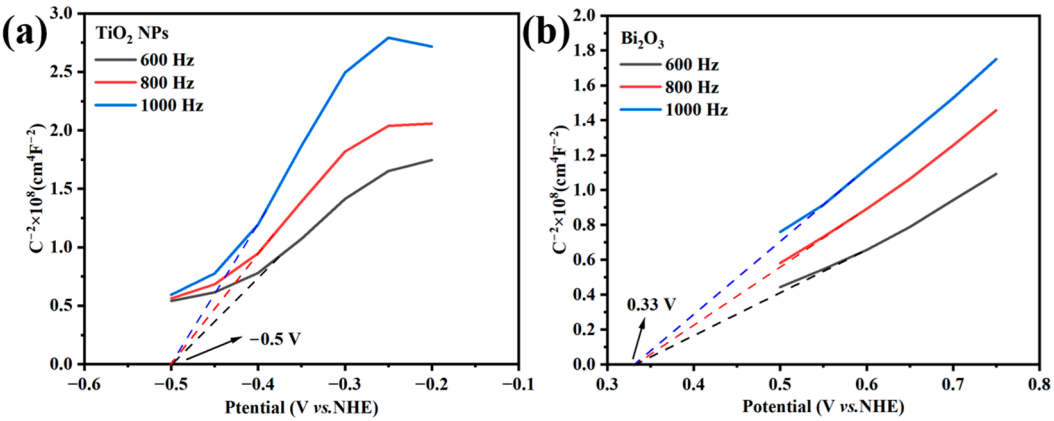

Figure 11. Mott–Schottky plots of (**a**) TiO_2 NPs and (**b**) Bi_2O_3.

Figure 12a,b shows the results from the free radical trapping experiments of TB-3. The addition of 1,4-benzoquinone (p-BQ), ethylenediaminetetraacetic acid disodium (EDTA-2Na) and tert-butanol (TBA) were used as trapping agents for superoxide radicals ($\cdot O_2^-$),

holes (h^+), and hydroxyl radicals (·OH) [37]. As displayed in Figure 12a, TC degradation over TB-3 without a trapping agent was 61.59%, while the TC degradation decreased to 32.32%, 55.43%, and 2.41% with the addition of EDTA-2Na, TBA, and p-BQ, respectively. Accordingly, the impact of free radicals on the degradation process was in the sequence of $\cdot O_2^-$ > h^+ > ·OH. In particular, $\cdot O_2^-$ was the main active substance in the photocatalytic oxidation degradation of TC over TB-3.

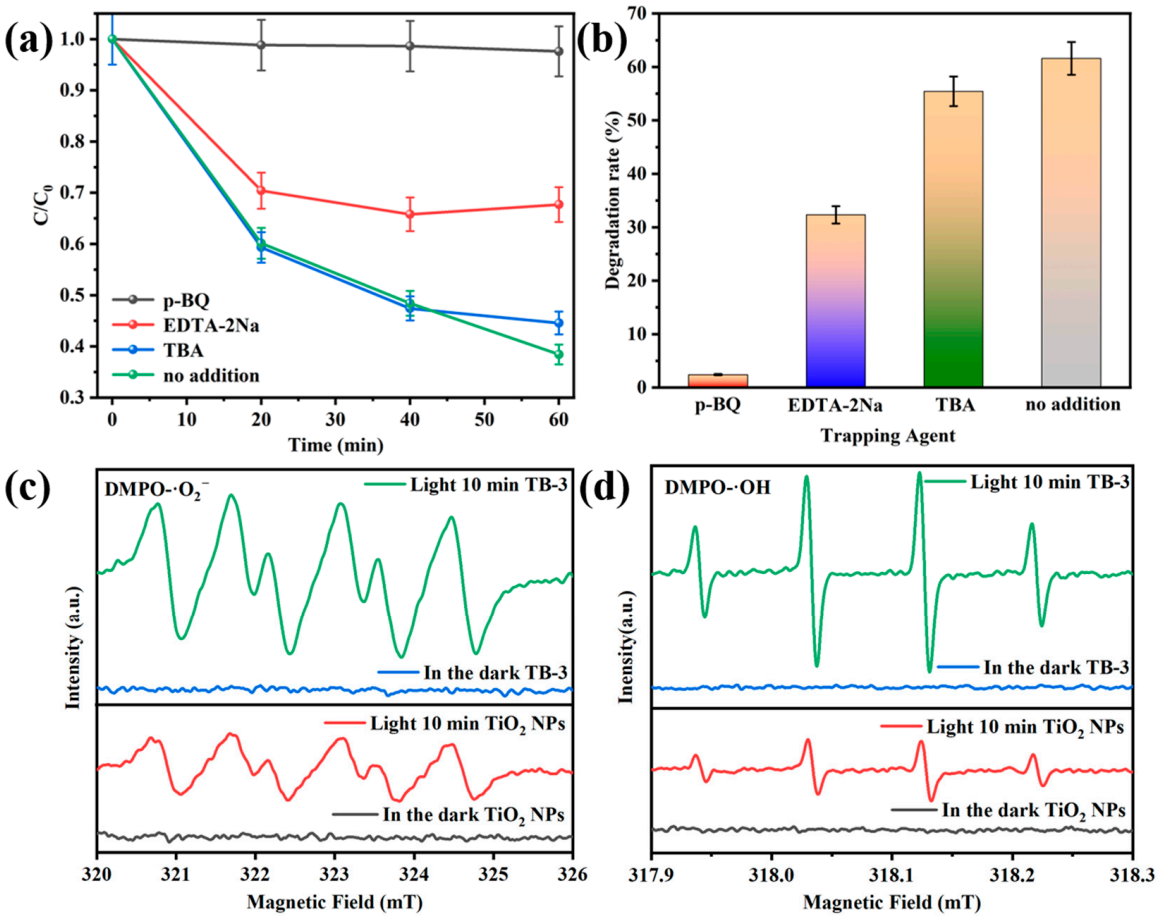

Figure 12. The effects of different scavengers on the degradation of TC over TB-3 (**a**,**b**). ESR spectra of (**c**) DMPO-·O_2^- and (**d**) DMPO-·OH.

The electron spin resonance (ESR) spectra of DMPO-·O_2^- and DMPO-·OH are displayed in Figure 12c,d. The DMPO-·O_2^- and DMPO-·OH signals revealed that no $\cdot O_2^-$ and ·OH were produced in the dark. However, characteristic peaks of DMPO-·O_2^- and DMPO-·OH were observed under visible light illumination, indicating that $\cdot O_2^-$ and ·OH are active substances in the photocatalytic process. It is worth mentioning that the DMPO-$\cdot O_2^-$ and DMPO-·OH signals of TB-3 were significantly enhanced compared with those of the TiO_2 NPs. This indicates that more $\cdot O_2^-$ and ·OH radicals can be generated when using TB-3 instead of TiO_2 NPs during photocatalysis.

Based on the above discussions, it can be clearly seen that the 0D/2D TiO_2 NPs/Bi_2O_3 heterojunctions were successfully fabricated and showed enhanced photocatalytic degradation and hydrogen evolution performances, which were proven by the results of XRD, FTIR, SEM/EDS, TEM, elemental mapping, and photocatalytic tests. The improvement in the photocatalytic activity of the 0D/2D TiO_2 NPs/Bi_2O_3 heterojunctions should be ascribed to the enhanced light absorption property, improved transfer and separation ability of photogenerated charge carriers, and reduced charge transfer resistance, as evidenced by the optical and electrochemical analysis. Furthermore, the generation of more $\cdot O_2^-$ and ·OH radicals over TB-3, which was found by the ESR results, was conducive to the boosted

photocatalytic degradation performance. Therefore, a proposed Z-scheme photocatalytic mechanism is described in Scheme 1 to explain the possible photocatalytic mechanism of TC degradation and hydrogen production over the TiO_2 NPs/Bi_2O_3 heterojunctions.

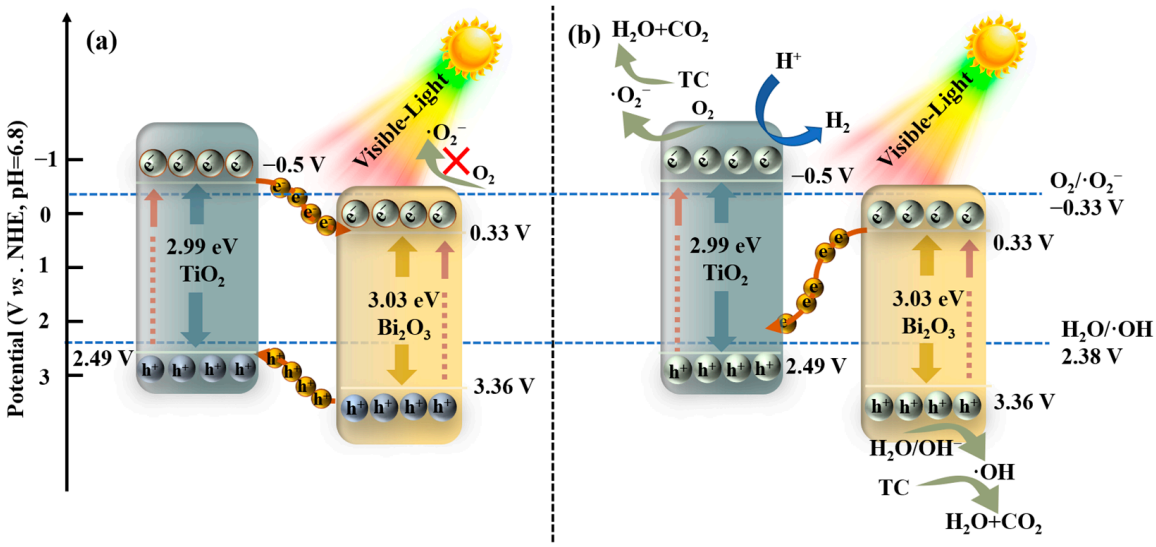

Scheme 1. Proposed mechanisms of the TiO_2 NPs/Bi_2O_3 (**a**) traditional type-II heterojunction and (**b**) Z-scheme heterojunction charge transfer pathway.

If the transfer of the photogenerated charge carriers follows the way of the traditional type-II heterojunction, the photogenerated electrons on the CB of the TiO_2 NPs will migrate to the CB of Bi_2O_3 due to the more negative CB value of the TiO_2 NPs than that of Bi_2O_3. Meanwhile, the holes located on the VB of Bi_2O_3 will transfer to the VB of the TiO_2 NPs. However, it was obvious that the electrons on the CB of Bi_2O_3 had an insufficient capability to produce $\cdot O_2^-$ radicals or hydrogen, since the CB potential of Bi_2O_3 was more positive than the redox potential of $O_2/\cdot O_2^-$ (−0.33 V vs. NHE) or H^+/H_2 (0 V vs. NHE) [49]. Furthermore, the ·OH radicals could not be generated either due to the less positive VB potential of the TiO_2 NPs than $H_2O/\cdot OH$ (2.38 V vs. NHE) [49]. These are inconsistent with the results from our free radical trapping experiments, hydrogen evolution, and ESR. Therefore, the traditional type-II heterojunction mechanism is not suitable to describe the charge transfer pathways of the TiO_2 NPs/Bi_2O_3 heterojunctions under visible light irradiation.

In contrast, a possible Z-scheme photocatalytic mechanism was proposed, as shown in Scheme 1b. Under visible light irradiation, the photogenerated electrons are excited from VB to CB in both Bi_2O_3 and the TiO_2 NPs. The photoinduced electrons on the CB of Bi_2O_3 will quickly transfer to the VB of TiO_2 to recombine with the holes, leaving the photogenerated electrons on the CB of the TiO_2 NPs and the remaining holes on the VB of Bi_2O_3. Because the CB potential of TiO_2 NPs (−0.5V vs. NHE) was more negative than the redox potential of $O_2/\cdot O_2^-$ (−0.33 V vs. NHE) and H^+/H_2 (0 V vs. NHE), the electrons on the CB of TiO_2 NPs could react with O_2 and H^+ to generate $\cdot O_2^-$ and H_2, which was evidenced by the active species trapping experiments and hydrogen evolution tests (Figures 10 and 12). Meanwhile, the holes on the VB of Bi_2O_3 could react with H_2O to produce ·OH radicals, as the VB potential of Bi_2O_3 was more positive than the redox potential of $H_2O/\cdot OH$ (2.38 V vs. NHE). Moreover, the holes as active species also had a sufficient oxidation capability to directly decompose TC [6,50]. In this way, the photogenerated charge carriers with relatively stronger oxidation and reduction ability can be efficiently separated, and more $\cdot O_2^-$ and ·OH active species can be produced to participate in photocatalytic degradation, as proven by ESR results (Figure 12c,d). Therefore, the above Z-scheme pathway of the charge transfer led to the significantly improved photocatalytic activity of TB-3.

3. Materials and Methods

3.1. Synthesis of TiO_2 NPs/Bi_2O_3 Composites

The preparation process of the TiO_2 NPs/Bi_2O_3 composites is shown in Scheme 2. TiO_2 NPs were prepared by a facile sol–gel method with the addition of F127 [51], which was used to modulate the particle size and inhibit the agglomeration of the synthesized TiO_2 NPs. Briefly, 1.6 g F127 was dissolved in 30 mL ethanol under stirring for 1 h. Subsequently, 3.5 mL $(CH_3CH_3CHO)_4Ti$, 0.74 mL concentrated HCl, and 2.3 mL CH_3COOH were added, followed by stirring for another 30 min. The resulting suspension was incubated in a Petri dish at 40 °C for 12 h, before being heated in an oven at 65 °C for 12 h to obtain a milky gel. Finally, the above materials were calcined in air at 450 °C) for 4 h to obtain TiO_2 NPs.

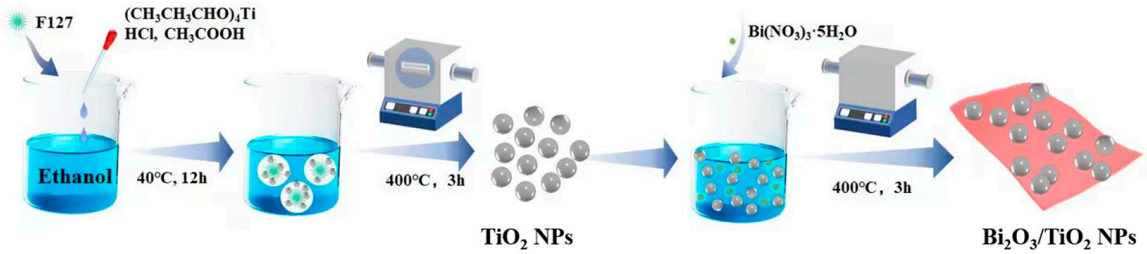

Scheme 2. Synthesis procedure of the Bi_2O_3/TiO_2 NP composites.

Afterward, 1 g of the above prepared TiO_2 NPs were added to 100 mL ethanol and dispersed by ultrasonication for 30 min. Then, a required amount of $Bi(NO_3)_3{\cdot}5H_2O$ was added and continuously stirred at 60 °C for 12 h. The resulting powders were dried at 110 °C overnight and calcined at 400 °C for 3 h to obtain a series of TiO_2 NPs/Bi_2O_3 composites. The final products were labeled as TB-x (x = 1, 2, 3, and 4), corresponding to the theoretical mass ratio of Bi_2O_3:TiO_2 = 5, 10, 15, and 20 wt%, respectively. For comparison, pure Bi_2O_3 was also synthesized using the same method without adding TiO_2 NPs.

3.2. Photocatalytic Performance Measurements

The photocatalytic performances of the TiO_2 NPs/Bi_2O_3 composites were investigated under visible light irradiation. A 300 W xenon lamp (PLS-SXE300, Perfect Light Company, Beijing, China) with a 420 nm cut-off filter was used to simulate visible light. Tetracycline hydrochloride (TC), a typical antibiotic, was chosen as the model pollutant to prepare antibiotic-containing wastewater. Typically, 30 mg of the catalyst was dispersed in a quartz reactor containing 50 mL TC with an initial concentration of 50 mg/L. The resulting suspension was stirred in the dark for 60 min to reach the adsorption–desorption equilibrium of TC over the catalyst, before exposure to the simulated visible light for another 60 min. During the reaction process, 3 mL of the suspension was sampled at regular intervals and then centrifuged to remove the catalyst. The residual TC in the supernatant was analyzed by a UV–Vis spectrophotometer (UV-8000, Shanghai Metash Instrument Co. Ltd., Shanghai, China) at the wavelength of 357 nm [52]. The blank test was also conducted in a similar manner to the above tests on the photocatalytic activity without a catalyst. In the trapping tests, the experimental procedures were similar to the above-mentioned tests, except with the addition of 1 mmol/L 1,4-benzoquinone (p-BQ), ethylenediaminetetraacetic acid disodium (EDTA-2Na), or tert-butanol (TBA) as the trapping agent for $\cdot O_2^-$, h^+, or ·OH, respectively.

The photocatalytic hydrogen evolution performances of the TiO_2 NPs/Bi_2O_3 composites were evaluated under visible light irradiation. Briefly, 50 mg of the catalyst was dispersed in 40 mL deionized (DI) water, before adding 10 mL methanol and 165 μL chloroplatin acid. Prior to irradiation, the above mixture was ultrasonically dispersed for 5 min. A 300 W xenon lamp (MC-PF300C, Beijing Merry Change Technology Co. Ltd., Beijing, China) with a 420 nm filter was utilized as the light source, and the light intensity was adjusted to 700 $mW{\cdot}m^{-2}$. Before illumination, the reaction system was pumped to vacuum,

and equipped with a circulating water cooling system to maintain the reaction system at 5 °C. The photocatalytic produced hydrogen was sampled every 30 min and measured by gas chromatography (GC7900, Tianmei, Shanghai, China), and the column and oven temperature was 25 °C.

4. Conclusions

In summary, 0D/2D TiO_2 NPs/Bi_2O_3 heterojunctions were successfully synthesized as efficient photocatalysts for TC degradation and hydrogen evolution under visible light irradiation. The optimal catalyst TB-3, synthesized with 15 wt% of Bi_2O_3/TiO_2 NPs, showed the highest TC photocatalytic degradation and hydrogen evolution. The apparent kinetic rate constant (k) of TB-3 was 8.15, 1.86, and 39 times greater than that of P25, TiO_2 NPs, and Bi_2O_3, respectively. The improvement in the photocatalytic activity of TB-3 resulted from the enhanced light absorption, improved transfer, and separation ability of the photogenerated charge carriers, the generation of more $\cdot O_2^-$ and ·OH radicals, and the Z-scheme charge transfer pathway of the TiO_2 NPs/Bi_2O_3 heterojunctions. This study provides a reference for the construction and optimization of Z-scheme 0D/2D heterojunctions as efficient visible light induced catalysts for photocatalytic applications.

Supplementary Materials: The following supporting information can be downloaded at: https://www.mdpi.com/article/10.3390/catal13030583/s1, Figure S1: FTIR spectra of TiO_2 NPs, Bi_2O_3, and TiO_2 NPs/Bi_2O_3 composites; Figure S2: EDS elemental analysis of TB-3 and table of the elemental content (inset); Figure S3: (a) Adsorption of TC in the dark, and (b) pseudo-second-order fitting plots of P25, TiO_2 NPs, and TB-3; Figure S4: Adsorption in the dark and photocatalytic degradation of TC under visible light irradiation; Figure S5: HPLC-MS spectra of intermediates in the photocatalytic degradation of TC using TB-3; Table S1: BET specific surface area (S_{BET}) and pore volume of the samples; Table S2: Kinetic fitting parameters of TC adsorption onto P25, TiO_2 NPs, and TB-3; Table S3. Comparison of TC removal % with other TiO_2 and Bi_2O_3-based heterojunctions. References [40–44] are cited in Supplementary Materials.

Author Contributions: Formal analysis, L.X., P.W. and W.H.; Investigation, L.X., P.W. and C.X.; Data curation, X.C. and Q.L.; Validation, W.H. and K.Y.; Writing—original draft preparation, L.X., P.W. and C.X.; Writing—review and editing, W.H. and H.H. All authors have read and agreed to the published version of the manuscript.

Funding: The research was supported by the Jiangxi Provincial Natural Science Foundation (20224ACB213010), the Jiangxi Provincial Education Department Project (GJJ200819), the Jiangxi Provincial Academic and Technical Leaders Training Program—Young Talents (20204BCJL23037), and the Qingjiang Excellent Young Talents of Jiangxi University of Science and Technology (JXUSTQJYX20170005).

Data Availability Statement: The authors confirm that the data supporting the findings of this study are available within the article and its Supplementary Materials. Derived data supporting the findings of this study are available upon reasonable request.

Conflicts of Interest: The authors declare no conflict of interest.

References

1. Ismael, M. Environmental remediation and sustainable energy generation via photocatalytic technology using rare earth metals modified g-C_3N_4. *J. Alloys Compd.* **2023**, *931*, 167469. [CrossRef]
2. Cheng, L.; Xiang, Q.-J.; Liao, Y.-L.; Zhang, H.-W. CdS-Based photocatalysts. *Energy Environ. Sci.* **2018**, *11*, 1362–1391. [CrossRef]
3. Li, P.; Wang, Y.; Huang, B.; Guan, S.; Luan, T.; Lin, G.; Yuan, K. Antibiotics in wastewater of Guangdong, China: Distribution patterns, and their environmental risk due to incomplete removal. *Sci. Total Environ.* **2022**, *849*, 157889. [CrossRef] [PubMed]
4. Imwene, K.-O.; Ngumba, E.; Kairigo, P.-K. Emerging technologies for enhanced removal of residual antibiotics from source-separated urine and wastewaters: A review. *J. Environ. Manag.* **2022**, *322*, 116065. [CrossRef] [PubMed]
5. Mishra, R.; Bera, S.; Chatterjee, R.; Banerjee, S.; Bhattacharya, S.; Biswas, A.; Mallick, S.; Roy, S. A review on Z/S–scheme heterojunction for photocatalytic applications based on metal halide perovskite materials. *Appl. Surf. Sci.* **2022**, *9*, 100241. [CrossRef]
6. Li, H.; Deng, F.; Zheng, Y.; Hua, L.; Qu, C.-H.; Luo, X.-B. Visible-light-driven Z-scheme rGO/Bi_2S_3-BiOBr heterojunctions with tunable exposed BiOBr (102) facets for efficient synchronous photocatalytic degradation of 2-nitrophenol and Cr(VI) reduction. *Environ. Sci. Nano* **2019**, *6*, 3670–3683. [CrossRef]

7. Derikvandi, H.; Nezamzadeh-Ejhieh, A. An effective wastewater treatment based on sunlight photodegradation by SnS_2 ZnS/clinoptilolite composite. *Solid State Sci.* **2020**, *101*, 106127. [CrossRef]
8. Yuan, Y.; Guo, R.-T.; Hong, L.-F.; Ji, X.-Y.; Lin, Z.-D.; Li, Z.-S.; Pan, W.-G. A review of metal oxide-based Z-scheme heterojunction photocatalysts: Actualities and developments. *Mater. Today Energy* **2021**, *21*, 100829. [CrossRef]
9. Xia, B.; Deng, F.; Zhang, S.; Hua, L.; Luo, X.; Ao, M. Design and synthesis of robust Z-scheme ZnS-SnS_2 n-n heterojunctions for highly efficient degradation of pharmaceutical pollutants: Performance, valence/conduction band offset photocatalytic mechanisms and toxicity evaluation. *J. Hazard. Mater.* **2020**, *392*, 122345. [CrossRef]
10. Jia, T.; Wu, J.; Xiao, Y.; Liu, Q.; Wu, Q.; Qi, Y.; Qi, X. Self-grown oxygen vacancies-rich CeO_2/BiOBr Z-scheme heterojunction decorated with rGO as charge transfer channel for enhanced photocatalytic oxidation of elemental mercury. *J. Colloid Interface Sci.* **2021**, *587*, 402–416. [CrossRef]
11. Jiang, T.; Wang, K.; Guo, T.; Wu, X.; Zhang, G. Fabrication of Z-scheme MoO_3/Bi_2O_4 heterojunction photocatalyst with enhanced photocatalytic performance under visible light irradiation. *Chin. J. Catal.* **2020**, *41*, 161–169. [CrossRef]
12. Li, Y.; Yu, B.; Liu, B.; Yu, X.; Qin, G.; Fan, M.; Zhang, Y.; Wang, L. Superior Fenton-like and photo-Fenton-like activity of MoS_2@ TiO_2/N-doped carbon nanofibers with phase-regulated and vertically grown MoS_2 nanosheets. *Chem. Eng. J.* **2023**, *452*, 139542. [CrossRef]
13. Farghali, A.-A.; Zaki, A.-H.; Khedr, M.-H. Control of Selectivity in Heterogeneous Photocatalysis by Tuning TiO_2 Morphology for Water Treatment Applications. *Nanomater. Nanotechnol.* **2016**, *6*, 12. [CrossRef]
14. Ma, Z.-Y.; Deng, L.-J.; Li, X.-B.; Fan, G. Preparation of TiO_2/Bi_2O_3 Microfibers and Their Photocatalytic Activity. *Chin. J. Chem. Phys.* **2014**, *27*, 439–444. [CrossRef]
15. Wang, Y.; Zhao, S.-Z.; Yang, Y.; Rodriguez, R.-D.; Lipovka, A.; Lu, Y.; Huang, H.-L.; Chen, J.-J. Ag nanoparticle-decorated Bi_2O_3-TiO_2 heterogeneous nanotubular photocatalysts for enhanced degradation of organic contaminants. *Colloids Surf. A Physicochem. Eng. Asp.* **2022**, *648*, 129233. [CrossRef]
16. Xu, C.; Zhou, Q.; Huang, W.-Y.; Yang, K.; Zhang, Y.-C.; Liang, T.-X.; Liu, Z.-Q. Constructing Z-scheme β-Bi_2O_3/ZrO_2 heterojunctions with 3D mesoporous SiO_2 nanospheres for efficient antibiotic remediation via synergistic adsorption and photocatalysis. *Rare Met.* **2022**, *41*, 2094–2107. [CrossRef]
17. Liu, Z.; Wang, Q.; Tan, X.; Zheng, S.; Zhang, H.; Wang, Y.; Gao, S. Solvothermal preparation of Bi/Bi_2O_3 nanoparticles on TiO_2 NTs for the enhanced photoelectrocatalytic degradation of pollutants. *J. Alloys Compd.* **2020**, *815*, 152478. [CrossRef]
18. Ke, T.; Shen, S.; Yang, K.; Lin, D. In situ fabrication of $Bi_2O_3/C_3N_4/TiO_2$@C photocatalysts for visible-light photodegradation of sulfamethoxazole in water. *Appl. Surf. Sci.* **2022**, *580*, 152302. [CrossRef]
19. Zhao, Z.-T.; Wang, N.; Zhang, H.; Shang, R.-M.; Xing, J.-J.; Zhang, D.; Li, J.-H. Fabrication of ZSM-5 zeolite supported TiO_2-NiO heterojunction photocatalyst and research on its photocatalytic performance. *J. Solid State Chem.* **2022**, *309*, 122895. [CrossRef]
20. Liu, X.-H.; Kang, Y.; Wang, Y. Novel high-efficiency visible-light-driven p-n heterojunction β-Bi_2O_3/Ag_2WO_4 photocatalysts. *Chem. Phys. Lett.* **2022**, *790*, 139347. [CrossRef]
21. Zhang, X.; Xu, G.; Hu, J.; Lv, J.; Wang, J.; Wu, Y. Fabrication and photocatalytic performances of BiOCl nanosheets modified with ultrafine Bi_2O_3 nanocrystals. *RSC Adv.* **2016**, *6*, 63241–63249. [CrossRef]
22. Liu, H.; Luo, M.; Hu, J.; Zhou, T.; Chen, R.; Li, J. β-Bi_2O_3 and Er^{3+} doped β-Bi_2O_3 single crystalline nanosheets with exposed reactive {001} facets and enhanced photocatalytic performance. *Appl. Catal. B* **2013**, *140–141*, 141–150. [CrossRef]
23. Ding, C.-K.; Qin, X.-W.; Tian, Y.-Y.; Cheng, B.-W. PES membrane surface modification via layer-by-layer self-assembly of GO@TiO_2 for improved photocatalytic performance. *J. Membr. Sci.* **2022**, *659*, 120789. [CrossRef]
24. Han, Z.-Z.; Wei, L.-Y.; Pan, H.-B.; Li, C.-Y.; Chen, J.-H. Variant effect of graphene sheets and ribbons on photocatalytic activity of TiO_2 sheets/graphene composite. *J. Mol. Catal. A Chem.* **2015**, *398*, 399–406. [CrossRef]
25. Hu, L.-M.; Dong, S.-Y.; Li, Q.-L.; Feng, J.-L.; Pi, Y.-Q.; Liu, M.-L.; Sun, J.-Y.; Sun, J.-H. Facile synthesis of BiOF/Bi_2O_3/reduced graphene oxide photocatalyst with highly efficient and stable natural sunlight photocatalytic performance. *J. Alloys Compd.* **2015**, *633*, 256–264. [CrossRef]
26. Zou, H.; Song, M.-X.; Yi, F.-C.; Bian, L.; Liu, P.; Zhang, S. Simulated-sunlight-activated photocatalysis of Methyl Orange using carbon and lanthanum co-doped Bi_2O_3–TiO_2 composite. *J. Alloys Compd.* **2016**, *680*, 54–59. [CrossRef]
27. Gao, X.-M.; Shang, Y.-Y.; Liu, L.-B.; Gao, K.-L. Ag plasmon resonance promoted 2D AgBr-δ-Bi_2O_3 nanosheets with enhanced photocatalytic ability. *J. Alloys Compd.* **2019**, *803*, 565–575. [CrossRef]
28. Rongan, H.; Haijuan, L.; Huimin, L.; Difa, X.; Liuyang, Z. S-scheme photocatalyst Bi_2O_3/TiO_2 nanofiber with improved photocatalytic performance. *J. Mater. Sci. Technol.* **2020**, *52*, 145–151. [CrossRef]
29. Hu, J.-D.; Xie, J.; Jia, W.; Zhang, S.; Wang, S.-Q.; Wang, K.; Cao, Y.-L. Interesting molecule adsorption strategy induced energy band tuning: Boosts 43 times photocatalytic Water splitting ability for commercial TiO_2. *Appl. Catal. B* **2020**, *268*, 118753. [CrossRef]
30. Limpachanangkul, P.; Liu, L.; Hunsom, M.; Piumsomboon, P.; Chalermsinsuwan, B. Application of Bi_2O_3/TiO_2 heterostructures on glycerol photocatalytic oxidation to chemicals. *Energy Reports* **2022**, *8*, 1076–1083. [CrossRef]
31. Li, L.; Dai, H.; Feng, L.; Luo, D.; Wang, S.; Sun, X. Enhance photoelectrochemical hydrogen-generation activity and stability of TiO_2 nanorod arrays sensitized by PbS and CdS quantum dots under UV-visible light. *Nanoscale Res. Lett.* **2015**, *10*, 418. [CrossRef] [PubMed]
32. Pan, D.-L.; Han, Z.-Y.; Miao, Y.-C.; Zhang, D.-Q.; Li, G.-S. Thermally stable TiO_2 quantum dots embedded in SiO_2 foams: Characterization and photocatalytic H_2 evolution activity. *Appl. Catal. B* **2018**, *229*, 130–138. [CrossRef]

33. Ren, C.-J.; Qiu, W.; Zhang, H.-L.; He, Z.-J.; Chen, Y.-Q. Degradation of benzene on $TiO_2/SiO_2/Bi_2O_3$ photocatalysts under UV and visible light. *J. Mol. Catal. A Chem.* **2015**, *398*, 215–222. [CrossRef]
34. Liu, Y.; Wei, J.-H.; Xiong, R.; Pan, C.-X.; Shi, J. Enhanced visible light photocatalytic properties of Fe-doped TiO_2 nanorod clusters and monodispersed nanoparticles. *Appl. Surf. Sci.* **2011**, *257*, 8121–8126. [CrossRef]
35. Jiang, Y.-B.; Sun, Z.-Z.; Chen, Q.-W.; Cao, C.; Zhao, Y.; Yang, W.-S.; Zeng, L.; Huang, L.-M. Fabrication of 0D/2D TiO_2 Nanodots/g-C_3N_4 S-scheme heterojunction photocatalyst for efficient photocatalytic overall water splitting. *Appl. Surf. Sci.* **2022**, *571*, 151287. [CrossRef]
36. Zhou, Q.; Huang, W.-Y.; Xu, C.; Liu, X.; Yang, K.; Li, D.; Hou, Y.; Dionysiou, D.-D. Novel hierarchical carbon quantum dots-decorated BiOCl nanosheet/carbonized eggshell membrane composites for improved removal of organic contaminants from water via synergistic adsorption and photocatalysis. *Chem. Eng. J.* **2021**, *420*, 129582. [CrossRef]
37. Li, J.; Yuan, H.; Zhu, Z. Improved photoelectrochemical performance of Z-scheme g-$C_3N_4/Bi_2O_3/BiPO_4$ heterostructure and degradation property. *Appl. Surf. Sci.* **2016**, *385*, 34–41. [CrossRef]
38. Liu, X.; Xu, Y.; Jiang, Y.; Song, M.; Liu, Z.; Guo, W.; You, L.; Wu, J.; Xu, M.; He, Y. Nanoarchitectonics of uniformly distributed noble-metal-free CoP in g-C_3N_4 via in-situ fabrication for enhanced photocatalytic and electrocatalytic hydrogen production. *J. Alloys Compd.* **2022**, *904*, 163861. [CrossRef]
39. Huang, W.; Tan, Y.; Zhang, C.; Zhou, Q.; Yang, K.; Zhang, Y.; Li, D.; Dionysiou, D.D. In situ decoration of $La(OH)_3$ on polyethyleneimine-linked dendritic mesoporous silica nanospheres targeting at efficient and simultaneous removal of phosphate and Congo red. *Environ. Sci. Nano* **2021**, *8*, 3792–3805. [CrossRef]
40. Wang, W.; Xiao, K.; Zhu, L.; Yin, Y.; Wang, Z. Graphene oxide supported titanium dioxide & ferroferric oxide hybrid, a magnetically separable photocatalyst with enhanced photocatalytic activity for tetracycline hydrochloride degradation. *RSC Adv.* **2017**, *7*, 21287–21297.
41. Che, H.; Chen, J.; Huang, K.; Hu, W.; Hu, H.; Liu, X.; Che, G.; Liu, C.; Shi, W. Construction of $SrTiO_3/Bi_2O_3$ heterojunction towards to improved separation efficiency of charge carriers and photocatalytic activity under visible light. *J. Alloys Compd.* **2016**, *688*, 882–890. [CrossRef]
42. Thanh Tung, M.-H.; Dieu Cam, N.-T.; Van Thuan, D.; Van Quan, P.; Van Hoang, C.; Thu Phuong, T.-T.; Lam, N.-T.; Tam, T.-T.; Phuong Le Chi, N.-T.; Lan, N.-T.; et al. Novel direct Z-scheme AgI/N–TiO_2 photocatalyst for removal of polluted tetracycline under visible irradiation. *Ceram. Int.* **2020**, *46*, 6012–6021. [CrossRef]
43. Zhang, S.; Yin, Z.; Xie, L.; Yi, J.; Tang, W.; Tang, T.; Chen, J.; Cao, S. Facet engineered TiO_2 hollow sphere for the visible-light-mediated degradation of antibiotics via ligand-to-metal charge transfer. *Ceram. Int.* **2020**, *46*, 8949–8957. [CrossRef]
44. Shi, Y.; Yan, Z.; Xu, Y.; Tian, T.; Zhang, J.; Pang, J.; Peng, X.; Zhang, Q.; Shao, M.; Tan, W.; et al. Visible-light-driven AgBr–TiO_2-Palygorskite photocatalyst with excellent photocatalytic activity for tetracycline hydrochloride. *J. Clean. Prod.* **2020**, *277*, 124021. [CrossRef]
45. Tan, Y.; Zhou, Q.; Huang, W.; Lu, K.; Yang, K.; Chen, X.; Li, D.; Dionysiou, D.-D. Highly efficient photocatalytic degradation over rose-like 1D/2D $La(OH)_3/(BiO)_2OHCl$ heterostructures boosted by rich oxygen vacancies and enhanced interfacial charge transfer. *Environ. Sci. Nano* **2023**, *10*, 215–228. [CrossRef]
46. Sun, H.; Xiao, Z.; Zhao, Z.; Huang, Y.; Zhai, S.; An, Q. Facile synthesis of $CaWO_4$ nanoparticles incorporated on porous carbons with improved photocatalytic degradation of tetracycline. *Colloids Surf. A Physicochem. Eng. Asp.* **2022**, *651*, 129790. [CrossRef]
47. Chen, P.; Dong, N.; Zhang, J.; Wang, W.; Tan, F.; Wang, X.; Qiao, X.; Keung Wong, P. Investigation on visible-light photocatalytic performance and mechanism of zinc peroxide for tetracycline degradation and Escherichia coli inactivation. *J. Colloid Interface Sci.* **2022**, *624*, 137–149. [CrossRef]
48. Li, D.; Liu, Y.; Yang, Y.; Tang, G.; Tang, H. Rational construction of Ag_3PO_4/WO_3 step-scheme heterojunction for enhanced solar-driven photocatalytic performance of O_2 evolution and pollutant degradation. *J. Colloid Interface Sci.* **2022**, *608*, 2549–2559. [CrossRef]
49. Cheng, L.; Xie, M.; Sun, Y.; Liu, H. Bi_2WO_6-wrapped 2D Ni-MOF sheets with significantly improved photocatalytic activity by a direct Z-scheme electron transfer. *J. Alloys Compd.* **2022**, *896*, 163055. [CrossRef]
50. Guo, Y.-C.; Yan, B.-G.; Deng, F.; Shao, P.-S.; Zou, J.-P.; Luo, X.-B.; Zhang, S.-Q.; Li, X.-B. Lattice expansion boosting photocatalytic degradation performance of $CuCo_2S_4$ with an inherent dipole moment. *Chin. Chem. Lett.* **2023**, *34*, 107468.
51. Li, Y.-L.; Han, X.-J.; Hou, Y.-Q.; Guo, Y.-P.; Liu, Y.-J.; Xiang, N.; Cui, Y.; Huang, Z.-G. In situ preparation of mesoporous Fe/TiO_2 catalyst using Pluronic F127-assisted sol-gel process for mid-temperature NH_3 selective catalytic reduction. *Chin. J. Catal.* **2017**, *38*, 1831–1841. [CrossRef]
52. Huang, G.; He, J.-X.; Zhang, X.; Feng, M.-M.; Tan, Y.; Lv, C.-C.; Huang, H.; Jin, Z. Applications of Lambert-Beer law in the preparation and performance evaluation of graphene modified asphalt. *Constr. Build. Mater.* **2021**, *273*, 121582. [CrossRef]